

Lawrence Berkeley National Laboratory

LBL Publications

Title

Surface Structural and Chemical Evolution of Layered $\text{LiNi}_{0.8}\text{Co}_{0.15}\text{Al}_{0.05}\text{O}_2$ (NCA) under High Voltage and Elevated Temperature Conditions

Permalink

<https://escholarship.org/uc/item/6m155394>

Journal

Chemistry of Materials, 30(23)

ISSN

0897-4756

Authors

Mukherjee, Pinaki
Faenza, Nicholas V
Pereira, Nathalie
[et al.](#)

Publication Date

2018-12-11

DOI

10.1021/acs.chemmater.7b05305

Peer reviewed

Surface Structural and Chemical Evolution of Layered $\text{LiNi}_{0.8}\text{Co}_{0.15}\text{Al}_{0.05}\text{O}_2$ (NCA) under High Voltage and Elevated Temperature Conditions

Pinaki Mukherjee,^{*,†} Nicholas V. Faenza,[‡] Nathalie Pereira,[‡] Jim Ciston,[§] Louis F. J. Piper,^{||} Glenn G. Amatucci,[‡] and Frederic Cosandey[†]

[†]Materials Science and Engineering, Rutgers University, Piscataway, New Jersey 08854, United States

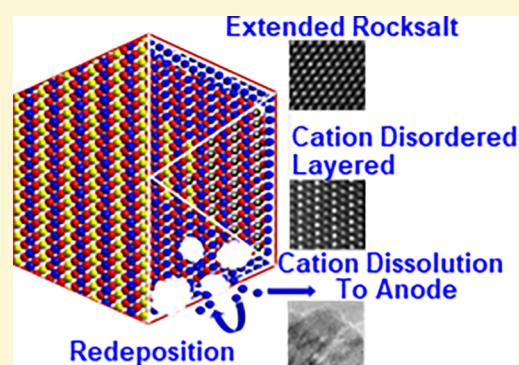
[‡]Energy Storage Research Group, Department of Materials Science and Engineering, Rutgers University, North Brunswick, New Jersey 08902, United States

[§]National Center for Electron Microscopy, Lawrence Berkeley National Laboratory, Berkeley, California 94720, United States

^{||}Materials Science and Engineering, Binghamton University, Binghamton, New York 13902, United States

S Supporting Information

ABSTRACT: This paper reports new insights into structural and chemical evolution of surface phases of $\text{LiNi}_{0.8}\text{Co}_{0.15}\text{Al}_{0.05}\text{O}_2$ (NCA) held at constant high voltages (up to 4.75 V) as well as high temperatures (60 °C) by correlating crystal structure using high angle annular dark field scanning transmission electron microscopy (HAADF-STEM) imaging with chemistry using electron energy loss spectroscopy (EELS). We also followed the Al distribution within individual NCA particles by X-ray energy dispersive spectroscopy (EDS). The progression of these phases as a function of distance from the edge shows simultaneous evolution of crystal structures and chemistry from rocksalt to layered, forming a complete solid solution. We have also observed an extended disordered phase with rocksalt ($\text{Fm}\bar{3}\text{m}$) symmetry in which quantitative electron energy loss spectroscopy reveals it to be an oxygen deficient cation disordered phase with chemical characteristics, as determined by EELS, similar to spinel. The formation of these disordered phases with cation and oxygen vacancies has been driven by surface oxygen loss caused by reactions with the electrolyte followed by cation migration from the octahedral 3a M (M = Ni, Co, Al) layer to the octahedral 3b Li layer. These surface rocksalt phases are not fully dense as they contain Al and Li as well as a high concentration of cation and oxygen vacancies. After discharge, Li is detected within these phases indicative that Li transport has occurred through these rocksalt phases. At 60 °C and 4.75 V a very large impedance rise is observed leading to complete cell irreversibility which is caused by significant metal dissolution from the cathode and formation of surface porosity. In the near surface region of some particles, a phase transformation from $\text{R}\bar{3}\text{m}$ (O3) to $\text{P}\bar{3}\text{m1}$ (O1) is also observed which has become thermodynamically stable from complete delithiation as well as from local Al surface depletion.



1. INTRODUCTION

Layered cathodes of the LiMO_2 type with M = Ni, Mn, and Co in various concentrations are now ubiquitous in portable electronics and electric vehicles^{1–4} and are now being introduced as large scale storage in support of intermittent solar and wind energy production. In order to maximize cyclability and safety, the charging voltage of cathodes in commercial settings is practically restricted to about 3.8–4.1 V, where approximately up to 0.6–0.7 of Li is extracted.^{5–7} As a consequence, only a fraction of the theoretical capacity is achieved. In order to realize the full potential of the cathode (i.e., to extract more Li from the layered cathode), higher voltages must be applied. At the present time a considerable amount of research is devoted toward narrowing the gap between practical and theoretical capacities.⁸ The degradation

mechanisms at the cathode and associated capacity fade in layered oxides have been reviewed in a series of articles.^{9–13} Among the main reasons for the capacity fading in layered cathodes, microcrack formation,^{14–17} surface phase transformation often associated with oxygen loss,^{18,19} and metal dissolution^{20–22} have received the most attention.

Among these, the formation of irreversible surface phases is of utmost interest as the process has been observed even after only the first cycle.²³ Most reports on surface phase changes point to a gradual change from layered structure to a spinel phase at the subsurface and finally to a rocksalt phase at the

Received: December 21, 2017

Revised: November 4, 2018

Published: November 5, 2018

surface.^{24–26} Although bulk formation of a spinel phase can occur during delithiation without oxygen loss^{27,28} via a 5 step diffusion process involving the migration of transition metal M (M = Ni, Mn, Co) into a tetrahedral site of the Li plane as well as Li migration to a tetrahedral site opposite to the vacancy left behind the migrating transition metal M, this leads to the formation of a transition state with the formation of a $\text{Li}_{\text{tet}}\text{-V}_{\text{oc}}\text{-Li}_{\text{tet}}$ dumbbell structure where V_{oc} is a M vacancy in the octahedral site with two Li_{tet} on opposite tetrahedral sites.^{11,28,29} Experimentally, bulk formation of spinel is rarely observed during delithiation from LiMO_2 to MO_2 even after extensive cycling.^{30,31} In general, spinel is found to nucleate preferentially at the surface³² either due to lower surface nucleation barrier or more likely from lower diffusion barrier caused by the presence of oxygen vacancies.³³ Therefore, one of the most debated aspects of the capacity fading process concerns the mechanisms for surface oxygen loss and its link to surface phase formation.^{34,35}

Thermal stability of layered positive electrode materials has been studied both theoretically³⁶ and experimentally,^{24–26,37–39} and a correlation between surface phase transformation and oxygen loss has been reported. This transformation occurs via formation of an intermediate spinel structure followed by the development of a rocksalt structure.^{24,25,37–39} Structural degradation and oxygen loss are dependent on the material's Li content and are observed to occur more rapidly and at lower temperatures when the cathode is fully delithiated, i.e. in the fully charged state. One possible reason is that the energy for oxygen vacancy formation decreases as Li content decreases resulting in an increase in the number of oxygen vacancies which in turn enable more transition metal movement, even at lower temperatures.⁴⁰

In the case of surface degradation via electrochemical processes, oxygen loss occurs via electrolyte–cathode reactions at the cathode surface.^{41,42} Similar to thermally induced degradation, surface phases first form by Li deintercalation followed by oxygen loss.⁴³ Upon loss of surface oxygen, the cation reduces to M^{2+} from M^{3+} or M^{4+} valence states which then migrates inward to occupy the vacant Li sites due to M^{2+} higher mobility compared to cations with higher valence states,³⁶ resulting in a disordered rocksalt cathode surface.

Several critical aspects of this transformation are not fully understood, such as, the onset voltage for the formation of surface phases (as a function of % Li extraction), the extent of these phases from the edge, and the need for the formation of a spinel phase as an intermediate phase from layered to rocksalt transformation. The phases formed in conjunction with oxygen loss are highly disordered containing a high fraction of metal and oxygen vacancies. There is considerable uncertainty in the literature as to the precise atomic structure and chemistry of these disordered surface phases, and they are often referred to as defect-spinel⁴⁴ or rocksalt⁴⁵ although with apparent similar atomic scale rocksalt image contrasts. It is interesting to note that the electron beam can induce changes in crystal structure from spinel to rocksalt⁴⁶ or from layered to rocksalt⁴⁷ with relatively minor changes in Li or O content. Surface phases can therefore have similar image contrast corresponding to $\text{Fm}\bar{3}\text{m}$ rocksalt symmetry but with drastically different chemistries that could range from MO to Li_xMO_2 and with different transition metal valence states. Li transport properties in disordered rocksalt phases have been studied recently by Ceder's group,⁴⁸ where they show that within a range of high

Li content, Li transport in cubic phases is indeed possible via percolation pathway.

In order to further our understanding of the surface phase formation in relation to transport properties, it is imperative to correlate the image contrast (structure) with local chemistry. The goals of this study are to determine the extent of the surface phase formation with respect to the oxygen content of the formed phases for cathodes held under high voltages up to 4.75 V and high temperature conditions (60 °C). In this study we have used the Ni-rich $\text{LiNi}_{0.8}\text{Co}_{0.15}\text{Al}_{0.05}\text{O}_2$ layered cathode (commonly known as NCA) as a model system, because it is viewed as a prominent layered cathode material with great commercial potential.^{1,6,49} In the present work we have studied surface phase evolution on delithiated samples held at constant voltage instead of the more traditional cycling in order to understand the impact of charge voltage (i.e., Li-content) content on cathode/electrolyte interfacial reactions and to prevent crack formation from repeated volume changes occurring during repeated intercalation and deintercalation processes.^{15,16}

In a companion paper, we reported the electrochemical properties of NCA held at high voltage up to 4.75 V and high temperature of 60 °C.⁵⁰ In the present paper, we report detailed surface chemical and structural evolution of NCA particles that have been exposed to the same extreme conditions. As the formation of surface phases is a very local phenomenon involving a small volume fraction of material and often not detectable by bulk X-ray or neutron scattering techniques, we used transmission electron microscopy (TEM) based techniques to characterize the surface phases formed on NCA cathode after aging at high voltages. Structural evolution, from particle edge to the interior, was measured by selected area diffraction (SAED), by high resolution TEM (HRTEM), as well as with high angle annular dark field scanning TEM (HAADF-STEM). For the chemical analysis determination of the phases, electron energy loss spectroscopy (EELS) as well as X-ray energy dispersive spectroscopy (EDS) was used.

2. EXPERIMENTAL PROCEDURES

2.1. Electrochemistry. $\text{LiNi}_{0.8}\text{Co}_{0.15}\text{Al}_{0.05}\text{O}_2$ (NAT1050, TODA America) tape electrodes were cast and Li-metal cells were assembled to measure the evolution at constant voltage. The NCA electrodes were fabricated using the Bellcore method.⁵¹ Casting slurries were a mixture of poly(vinylidene fluoride-co-hexafluoropropylene) (PVDF-HFP, Kynar 2801, Elf Atochem), carbon black (Super P (SP), MMM), propylene carbonate (Aldrich), and acetone (Aldrich). Homogenous slurries were cast and allowed to air-dry, and then the propylene carbonate plasticizer was extracted by soaking the tape in anhydrous diethyl ether (Aldrich). Electrodes were cast with a composition of 88.81 wt % active material, 3.91 wt % SP, and 7.28 wt % PVDF-HFP. All electrodes were dried at 120 °C under vacuum for a minimum of 10 h, and stored in an Ar-filled glovebox to avoid atmospheric exposure.

All materials evaluated by microscopy were tested in powder form because of the absence of PVDF-HFP binder in the powder cells^{52–54} allows elimination of any signal interference and possible chemical reactions. The NCA and carbon black materials were dried under vacuum at 100 °C for 2 h and at 120 °C overnight, respectively, prior to mixing in an argon-filled glovebox using a mortar and pestle. Mixtures encompassed 97.5 wt % NCA and 2.5 wt % SP.

Electrochemical tests were performed versus lithium metal in 2032 coin cells (Hohsen) using Celgard and glass fiber separators soaked with 1 M LiPF_6 in ethyl carbonate (EC):dimethyl carbonate (DMC) at 50:50 in vol % electrolyte (BASF). Cycling was conducted using a VMP3 (Biologic) or a Maccor battery cycling system. The cells were

typically charged at 10 mA/g, up to three different cutoff voltages of 4.1, 4.5, and 4.75 V, held at constant voltage for 2 weeks, and then discharged to 2.7 V, all at 24 °C. Samples were also tested at 60 °C with charge up to 4.75 V at 25 mA/g with potentiostatic steps for 10 and 150 h, respectively. These samples were not discharged. Finally, the impedance cells were charged galvanostatically at 25 mA/g to either 4.1, 4.5, or 4.75 V and then held potentiostatically while electrochemical impedance spectroscopy⁴² scans were run every 12 h. All EIS experiments were controlled by the VMP3 in a frequency range of 400 kHz to 15 mHz with a sinusoidal amplitude of 20 mV.

2.2. Transmission Electron Microscopy. Because of the air and moisture sensitivity of NCA, all the TEM sample preparations were done in an Ar filled glovebox. The O₂ and H₂O levels in the glovebox were both below 0.5 ppm. The cathode materials held at high voltages were first extracted from the powder coin cell described above. These binder-free NCA powders were then gently ground in dimethyl carbonate (DMC) solution using a mortar and pestle in a glovebox with Ar atmosphere. The NCA powder, with primary particles 300–400 nm in size, is composed of large 10–20 μm agglomerates that are too thick to be electron transparent. Very low energy grinding was necessary to break the agglomerates without destroying the individual particles and surface structures. Occasional particle fracturing of individual particles can occur, but these particles are easily discernible from others due to their sharp and thick edges and were discarded from further observations. The ground powders were suspended in DMC and drop cast onto 200 mesh holey C grids. The grids were then placed in a vial and sealed. The only time the samples were exposed to air was during the final transfer to the TEM which was always limited to less than 2 min. This short amount of exposure did not change the surface crystal structure or chemistry, as evident from the absence of any detectable Li₂CO₃ or LiOH at the surface by HRTEM and EELS. HRTEM and SAED were carried out with a JEOL 2010F TEM/STEM microscope operated at 197 kV. The HAADF STEM imaging and EELS experiments were performed using a field emission aberration corrected FEI Titan STEM operated at 300 kV (commonly known as TEAM I) at National Center for Electron Microscopy at Lawrence Berkeley National Laboratory. The spatial resolution of the HAADF-STEM system was 0.07 nm. The EELS experiments were conducted with a Gatan Tridiem spectrometer with an energy resolution of 0.8 eV. The convergence and collection semi angle of the EELS detector were 17 and 23 mrad, respectively. The EDS spectroscopy was performed at Brookhaven National Laboratory (BNL) using a FEI Talos microscope operated at 200 kV and fitted with Bruker SuperX EDS quad detectors. Due to its efficient design, getting fast nanometer resolution X-ray maps with high counts is easily achievable. The data were analyzed using a Gatan Digital Micrograph. The X-ray maps were analyzed using Bruker Esprit software. Quantitative analysis of diffraction patterns and HAADF-STEM simulations were performed with JEMS software provided by P. Stadelmann.

In this study, we are making observations through whole particles with unknown thickness variations from the edge and with resulting images having an overlap between transformed surfaces and interior. The HAADF and EELS results reported in this study assume a constant thickness variation along the beam direction and represent an upper limit in the extent of phase transformation due to the overlap between the transformed surfaces and the bulk.

3. RESULTS

3.1. Electrochemistry. The NCA cathodes were charged to and held under potentiostatic conditions at 4.1, 4.5, and 4.75 V for 2 weeks followed by discharge to 2.7 V. Table 1 summarizes the Li content of these samples. Upon constant current charge to 4.1, 4.5, and 4.75 V at room temperature the Li content decreased to 0.35, 0.16, and 0.10 Li, respectively. After the 2 weeks aging process, the Li content is further reduced to 0.11 when held at 4.1 V and 0.05 for 4.5 and 4.75 V. After discharging (lithiation) to 2.7 V, the Li content

Table 1. Electrochemical Measurement Conditions of NCA Samples Studied in This Work^a

| Voltage (V) | Time at CV (h) | Temp. (C) | Sample SOC | Lithium Content | | |
|-------------|----------------|-----------|------------|---------------------------|-------------|------------------------------|
| | | | | End of Charge Cst Current | Cst Voltage | End of Discharge Cst Current |
| 4.1 | 366 | 24 | Discharged | 0.35 | 0.11 | 0.71 |
| 4.5 | 366 | 24 | Discharged | 0.16 | 0.05 | 0.82 |
| 4.75 | 336 | 24 | Discharged | 0.10 | 0.05 | 0.81 |
| 4.75 | 10 | 60 | Charged | 0.08 | 0.05 | |
| 4.75 | 150 | 60 | Charged | 0.08 | 0.05 | |

^aAll samples were aged electrochemically under constant voltage conditions and then discharged to 2.7 V, except at 60 °C where the reaction in the cell and resulting high impedance prohibited re-lithiation. The table shows holding voltage, time at constant voltage (CV), temperature, and Li content at the end of charge, at the end of voltage hold, and after discharge.

increased to 0.71, 0.82, and 0.81 for 4.1, 4.5, and 4.75 V respectively (cf. Table 1). A schematic LiMO₂-MO₂-MO ternary phase diagram (with M = Ni, Co, Mn) is shown in Figure 1. These Li contents for the three charge voltages are

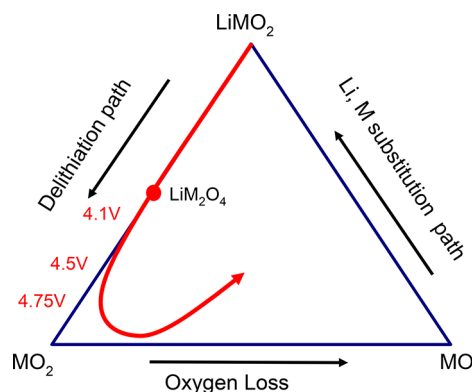


Figure 1. Ternary phase diagram with schematic representation of the three reaction paths; (1) delithiation from LiMO₂ to MO₂, (2) oxygen loss from MO₂ to MO, and (3) Li/M substitution paths from MO to LiMO₂ with M representing Ni, Mn, or Co. The arrow represents a possible path after charge, aging, and discharge process.

represented along the LiMO₂ to MO₂ line of the ternary phase diagram of Figure 1. Upon delithiation, the path from LiMO₂ to MO₂ is concurrent with transition metal cations valence increasing to M⁴⁺ from M³⁺. If oxygen loss is occurring after delithiation, then the phases will follow the MO₂ to MO path. If both delithiation and oxygen loss occurs simultaneously, the Li, M substitution path will be followed. Without oxygen loss, the path after discharging would remain along the MO₂ to LiMO₂ line, but as some oxygen loss is expected due to the combination of the charging, aging (oxygen loss), and discharging processes, the cathode will follow a path represented schematically by the red arrow terminating somewhere inside the ternary phase diagram.

Total impedance development with time as determined by EIS for the NCA cells with potentiostatic voltage holds at 4.1, 4.5, and 4.75 V is shown in Figure 2. The detailed results of the respective changes in electrochemistry are reported in a companion paper.⁵⁰ Two cells were tested at each voltage and

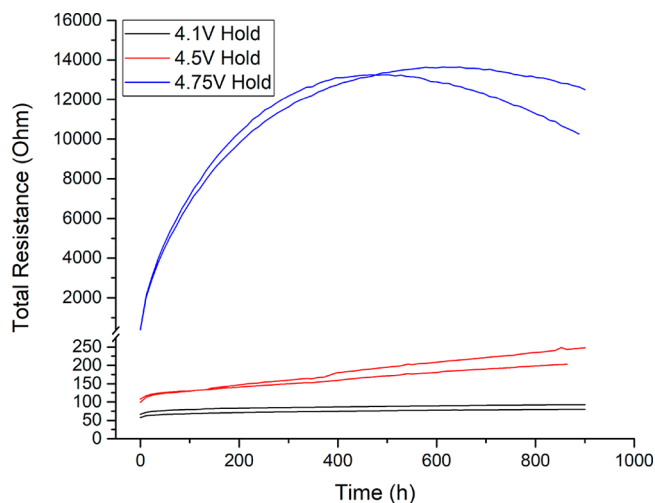


Figure 2. Total impedance development as a function of time for three hold voltages of 4.1, 4.5, and 4.75 V. Two sets of measurements were performed at each voltage, showing the good reproducibility of the data.

show the good reproducibility of the data. At 4.75 V, the total impedance dramatically increases compared to 4.1 or 4.5 V. At 4.1 V the impedance saturates at 75 Ohm, and at 4.5 V it increases linearly up to 150 Ohm after 650 h of aging. In contrast, at 4.75 V the impedance increases dramatically to over 12 kOhm.

3.2. Surface Phase Evolution at 4.1, 4.5, and 4.75 V and RT. The crystal structure of pristine NCA is $R\bar{3}m$. It is a rhombohedral unit cell with $a = 0.2864$ nm and $c = 1.4171$ nm (represented as hexagonal axes). It has cubic close packing of O atoms along the z axis with Li in the 3b octahedral sites and transition metal atoms M ($M = \text{Ni, Co, Al}$) occupying the 3a octahedral sites.⁵⁵ In the case of the spinel structure, 33% of

the M ions have migrated to the Li layer and occupy alternative Li sites (cf. Figure 3b). This alternative occupancy of the Li sites is a characteristic feature of the spinel phase, which can be clearly identified by HAADF-STEM. In the spinel phase, the Li atoms migrate from the octahedral site to occupy the tetrahedral sites leaving only the M atoms occupying the octahedral sites.⁵⁶ The periodic occupation of M atoms in Li sites gives rise to a second set of $\{111\}$ planes (two variations of the four $\{111\}$ planes) with $d = 0.47$ nm and inclined at 58° with respect to each other. This extra set of planes gives rise to extra reflections characteristic of spinel when viewed along the $[110]_C$ direction. The rocksalt structure ($Fm\bar{3}m$) forms when M atoms occupy all octahedral sites randomly (cf. Figure 3c). In this paper, the spinel nomenclature is reserved to structures or images that respect the $Fd\bar{3}m$ space group symmetry observed in either the SAED pattern or FFT taken from high resolution S/TEM images and similarly for the nomenclature of the $Fm\bar{3}m$ rocksalt phase. As mentioned in the introduction, the layered or spinel phase can easily transform, after high electron beam exposure, into a rocksalt phase by a simple disordering without significant changes in chemistry, transition metal valence state, or local electronic structure.^{46,47} Figure 3 shows typical diffraction patterns (SAED) from the near surface region of NCA particles taken from cathodes held for 2 weeks at 4.1, 4.5, and 4.75 V. For each condition approximately 25 particles were searched and then the best small ones without overlap with each other or with carbon support were oriented along the $[110]_L$ zone axis of the layered ($R\bar{3}m$) unit cell. At 4.1 V (Figure 3d) the diffraction pattern corresponds to the layered $R\bar{3}m$ structure implying that the original structure has not transformed. At 4.5 V, (Figure 3e) extra diffraction spots from two sets of extra $\{111\}$ reflections from the spinel phase ($Fd\bar{3}m$) appear. At 4.75 V (Figure 3f) the diffraction pattern contains reflections originated from superposition of rocksalt and layered structures. The rocksalt reflections are

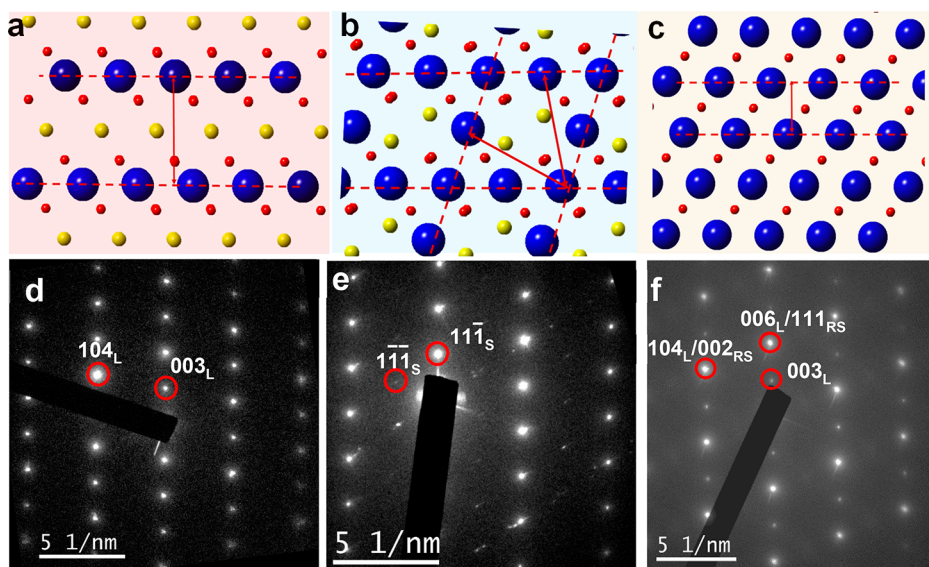


Figure 3. (Top row). Projections of crystal structure of NCA along the $[110]$ zone axis. The topotactic phase transformation from (a) rhombohedral ($R\bar{3}m$) to (b) cubic spinel ($Fd\bar{3}m$) and to (c) rocksalt ($Fm\bar{3}m$) can be visualized along this $[110]$ zone axis, with cation migration from 3a (M) to 3b (Li) position in the layered structure. The yellow, red, and blue spheres represent Li, O, and metal (Ni, Co, Al) atoms, respectively. (bottom row) Selected area electron diffraction of NCA held for 2 weeks at (d) 4.1 V, (e) 4.5 V, and (f) 4.75 V. The near surface structure remains (d) $R\bar{3}m$ layered at 4.1 V, (e) $Fd\bar{3}m$ spinel phase appears at 4.5 V, and (f) the strong and weak modulating reflections show the presence of ($Fm\bar{3}m$) rocksalt phase along with the layered ($R\bar{3}m$) phase.

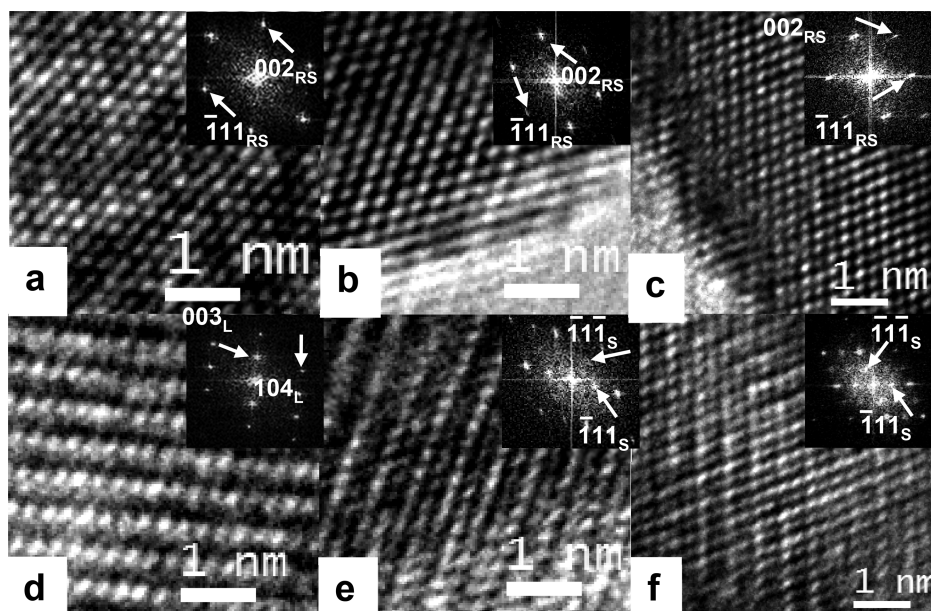


Figure 4. HRTEM images and corresponding FFT of surface region (a–c) and near surface (d–f) region in NCA aged for 2 weeks at 4.1 V (a, d) 4.5 V (b, e) and 4.75 V (c, f) (from left to right). The rocksalt ($Fm\bar{3}m$) contrast is present in all three surfaces. The subsurface region remains (R3m) layered at 4.1 V while, there is some evidence of spinel at 4.5 V and to a lower extent at 4.75 V.

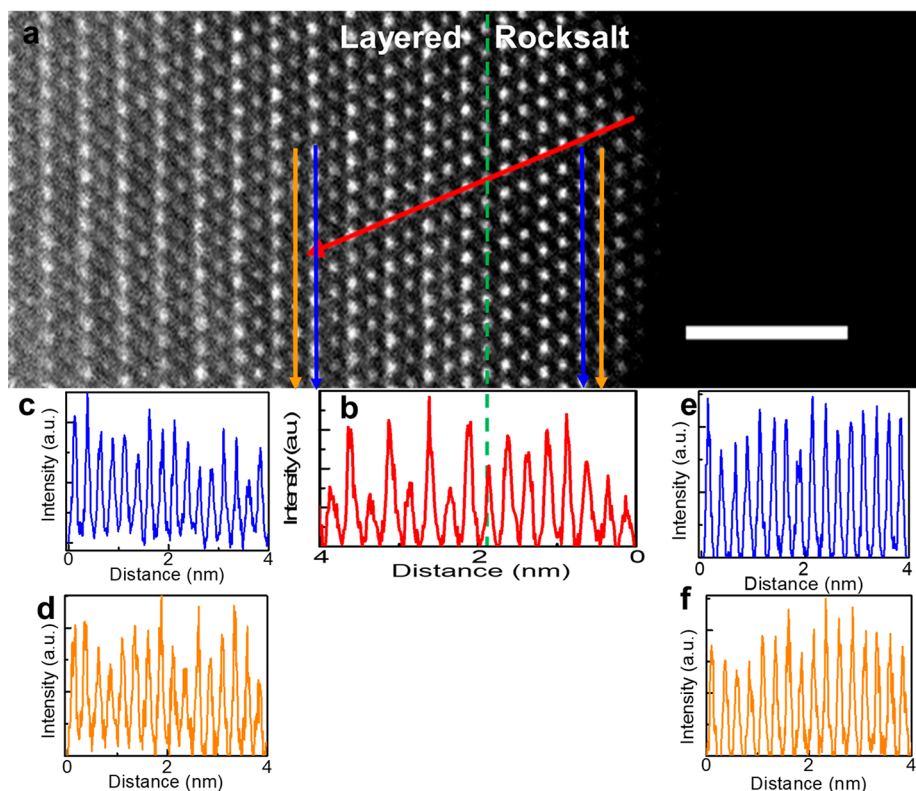


Figure 5. (a) High resolution HAADF STEM image of NCA held at 4.75 V for 2 weeks. (b) The profile at the bottom (red) of the image is drawn across atom columns. The image shows transformation from a layered-like contrast to a rocksalt-like contrast at edge of the particle. (c–f) The blue and yellow lines correspond to intensity profiles along columns of Ni atoms in its original position (3a) and in Li positions (3b) with respect to a rhombohedral crystal structure. The lines on the left (c, d) and right (e, f) are drawn in layered and rocksalt areas, respectively. Scale bar is 2 nm.

coincident with those of the layered structure (for instance: $(006)_L // (\bar{1}11)_{RS}$ or $(104)_L // (002)_{RS}$).

To understand the local variations of crystal structures, HRTEM images were obtained from the particles oriented along the $[110]_L$ zone axis. Figure 4 shows the HRTEM

images taken from surface and subsurface regions. For the sake of consistency, the region within the first 5 nm from the edge of the particle is considered as surface. At all voltages, the HRTEM images from the surface show rocksalt structure (cf. Figure 4a–c). At 4.1 V, this rocksalt-like contrast is not

observed by SAED pattern as it is confined to very narrow and isolated regions near the edge of the particle. The rocksalt contrast near the edge is more prominent at 4.5 and 4.75 V although not always continuous. The images from the subsurface regions presented in Figures 4d–f were taken from approximately 10 nm from the edge. At 4.1 V the subsurface region shows the layered-like contrast with characteristic presence of $(003)_L$ reflections. The fast Fourier transform (FFT) image shows spots corresponding only to the layered structure. At 4.5 V, the image shows a doubling of the contrast periodicity with FFT spots originating from $\{111\}$ reflections of spinel structure. The HRTEM images are in agreement with electron diffraction results (Figure 3b). At 4.75 V the subsurface structure appears to contain more rocksalt, and in some area the FFT shows extra spots corresponding to spinel structure.

In some areas of the particles, the rocksalt contrast observed at 4.75 V extended well beyond 20 nm. From a structural point of view, the extent of this rocksalt-like contrast increases with charging voltage and with the duration of the voltage, becoming prominent at 4.75 V while the presence of spinel phase greatly decreased.

The extent of this rocksalt-like contrast at 4.5 and 4.75 V was further investigated by atomic resolution STEM imaging using a high angle annular dark field (HAADF) detector. In this imaging mode, the atomic image contrast is proportional to $Z^{2-\delta}$ with the factor δ dependent on microscope parameters such as dark field detector inner and outer diameters.^{57–59} The intensity within each atomic column in the image is a measure of number of transition metal M (M = Ni and Co) atoms and vacancies present along the atomic column. The atomic scattering from Li and O is too weak to provide any contrast and is not visible by HAADF STEM. Similarly, Al atoms are not expected to contribute significantly to the image contrast. In the HAADF-STEM imaging, the layers containing Li atoms would therefore appear black and any migration of M atom from 3a to 3b Li sites is directly observable. The resolution limit of the instrument (0.07 nm) is sufficient to also resolve atomic migration to the tetrahedral site as well. In view of the higher mobility of Ni atoms (especially in the Ni^{2+} state) as compared to Co and Al, we can assume that most of the filling of the 3b Li site is done with Ni atoms and we discuss qualitatively the large variations in image contrast in terms of the number of Ni atoms along the imaging column. As the STEM contrast is a nonlinear function of number of atoms in a column, we have simulated the HAADF image of LiNi_2O_4 ($\text{Fd}\bar{3}m$) spinel along the $[110]_s$ for three different thicknesses (5.8 nm, 10.4 nm, 23.2 nm). Viewed along the $[110]_s$ direction, the spinel structure has characteristic Ni atomic columns containing 0, 2, and 4 Ni atoms per unit cell (c.f. Supporting Information Figure S1). The intensity ratio between the atomic column with 2 and 4 Ni per cell increases as a function of thickness and becomes proportional to the number of Ni atoms at about 25 nm.

A high resolution HAADF-STEM image of NCA held at 4.75 V for 2 weeks is shown in Figure 5a. It reveals a layered-like contrast with increasing amount of transition metal M occupying the Li positions as we approach the particle edge. A rocksalt-like contrast is observed within the first 1–2 nm from the edge, and it becomes layered-like above 2 nm. The intensity profile taken across the atom columns (follow red arrow and profile) is shown at the bottom of the image (5b). In the rocksalt-like region, the intensity of Ni atoms in the Li

layer (3b) and Ni in its original layer (3a) is the same. Qualitatively, this amounts to uniform occupancy of Ni in its original and in the Li layer. Above 2 nm the Li layers are only partially filled by Ni. A quantitative analysis from this region shows that the relative intensity of Ni in the Li layer and Ni in the original Ni layer is 0.3. As the STEM contrast is thickness dependent, it is very hard to determine the exact amount of Ni movement. It is, however, interesting to note that similar contrast was observed for a 5.8 nm thick spinel supercell (cf. Supporting Information Figure S1). However, unlike for the spinel structure, all octahedral sites are occupied randomly instead of ordered in alternate Li sites as shown in Figure 3d. In addition, the movement of ion M from its original site (3a) to the neighboring Li (3b) site is not a uniform process. The intensity profiles at the left (Figure 5c, d) and right (Figure 5e, f) of the image which are from layered and rocksalt areas, respectively, show large variations in intensity in the order of 10 to 15%. The intensity variations along these layers imply variations in the number of M, suggesting the creation of large number of M vacancies within these layers.

At 4.75 V, a different extended contrast has been observed as shown in Figure 6. In this area, the corresponding atomic

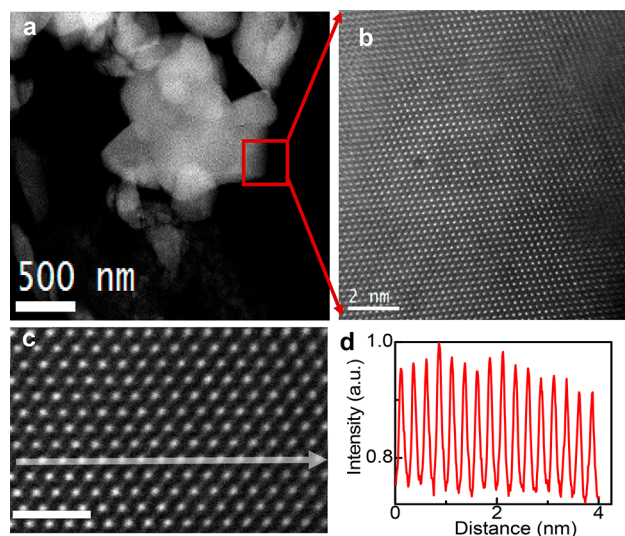


Figure 6. (a) Low magnification HAADF STEM image of NCA held at 4.75 V for 2 weeks and (b) corresponding high resolution HAADF STEM image revealing a rocksalt-like contrast. (c) Higher magnification within (d) the corresponding intensity profile from the arrow region. (The marker in (c) is 1 nm.)

HAADF-STEM image (Figure 6b) reveals a rocksalt type contrast which spread beyond 20 nm from the particle edge. The higher magnification image (Figure 6c) with the corresponding intensities profile (Figure 6d) reveals a filling of octahedral sites. Also, it can be viewed that the intensity profile is not uniform, indicating variations in the number of transition metals (or vacancies) along each specific atomic column. Up to 20% variation in the number of transition metals can be estimated from Figure 6d.

It has been pointed out that a distinction between layered and rocksalt phases is not straightforward and that for some zone axis orientations, the two phases are undistinguishable.^{60,61} For instance, a rocksalt contrast along the $[110]_R$ zone axis is very similar to that of $[421]_L$ of layered structure. In our experiments, all the particles studied were first oriented

along the $[110]_L$ zone axis of the layered structure. The rocksalt phase that we observed grows topotactically in a $[110]_R$ zone axis alongside a layered structure oriented along $[110]_L$. An example of a single particle containing adjacent layered and rocksalt contrasts is shown in Supporting Information Figure S2. Areas with rocksalt contrast can be present in a particle as one of the four orientation variants of the layered structure.⁶⁰ These domains are usually marked by domain boundaries where preferential segregation of Ni occurs.⁶¹ In the present study, we are describing a separate rocksalt phase, which is different from an orientation domain. It is to be mentioned here that the phases we find in NCA are topotactic and the extended rocksalt phase is found to occur as a result of extensive disordering of the layered structure. The main distinguishing feature between these phases is the presence of $\{003\}$ reflections in the layered structure that originates from layer ordering and slight distortions of the parent rocksalt structure along the four diagonals, i.e. along $\langle 111 \rangle$. Therefore, it can only be visualized along some specific directions such as, $[110]$, $[1\bar{1}0]$, and $[210]$. To identify the contrasts clearly as a separate phase, we performed tilting experiments and looked into the rocksalt and layered contrasts from three different orientations. The results are presented in Supporting Information Figure S3. In this figure we have identified two transformed areas, ROI 1 and ROI 2, and observed them along the $[121]$, $[210]$, and $[110]$ zone axis with respect to the layered structure. Along the $[121]$ direction the RS and layered contrasts are indistinguishable as the $\{003\}$ reflections are not present along this direction. Along the $[210]$ and $[110]$ directions, however, the RS and layered contrast are easily distinguishable. As we tilt the particle along the layered $[121]$, $[210]$, and $[110]$ zone axis, the corresponding contrast changes in the RS area correspond to the $[111]$, $[121]$, and $[110]$ zone axes of the cubic structure, respectively. This clearly shows that the contrasts we present here originate from different phases. The volume fraction of the extended rocksalt phases has been estimated by direct ADF-STEM imaging at less than 5%. Such estimation is difficult to confirm by X-ray diffraction as the first six reflections of the RS phase (111, 200, 220, 311, 222, and 400) are coincident with the layered reflections.

The extent of surface phase transition has been measured from the intensity ratio of M ($M = \text{Ni}$ and Co) in the original Ni 3a layer and M in the Li 3b layer as a function of distance for a different particle surface. The ratio would vary from 0 to 1 corresponding to a perfect layered structure and a completely disordered rocksalt structure, respectively. In Figure 7 curves 1 and 2 correspond to measurements made on 4.5 V aged

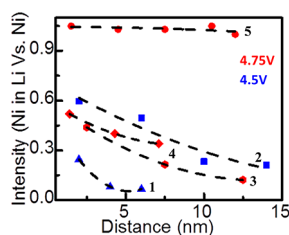


Figure 7. Extent of phase transformation in NCA aged at 4.5 and 4.75 V. The curves measure the intensity ratio of transition metal M in the Li layer relative to the intensity of M in the M layer. Series 1 and 2 are measurements from cathodes held at 4.5 V while series 3, 4, and 5 are from cathodes held at 4.75 V.

samples while curves 3, 4, and 5 correspond to measurements made on 4.75 V aged samples. There is some inhomogeneity from particle to particle but in general the extent of Ni and Co occupation into the Li layer is greater for aging at 4.75 V and extends beyond 10 nm.

The HAADF-STEM results reveal considerable transition metal migration as well as structural disordering. We have used EELS in order to gain insight into the role of oxygen loss, as well as the local chemical environment and valence state of the transition metals as a function of the observed surface structural changes. As a general principle, the thinnest edges of the particles were chosen for both STEM imaging and EELS measurements. Moreover, all EELS measurements were carried out within the first 10 nm from the edge of the particles, thus minimizing the chance of variation due to thickness while interpreting EELS spectra. The characteristic EELS features of the oxygen-K and Ni-L edges for NCA and NiO are shown in Figures 8a and Figure 8b, respectively. The data were collected by scanning the beam over a 2×20 nm with a total dose of $4.7 \times 10^5 \text{ e}^-/\text{Å}^2$.

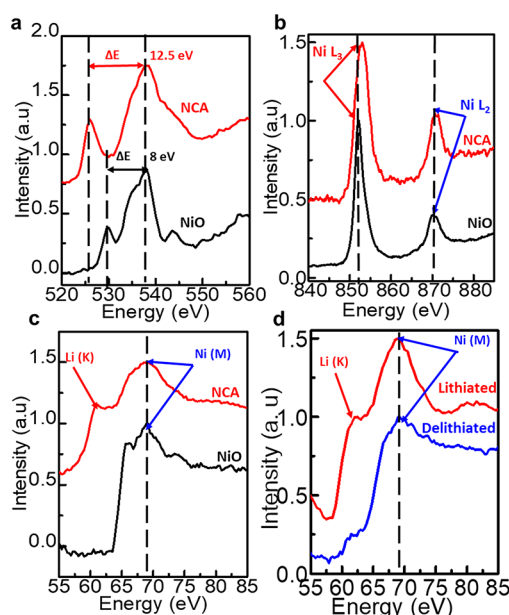


Figure 8. (a) EELS O–K edge spectra for pristine NCA and NiO. The separation between the oxygen pre and main peak is 12.5 and 8 eV for NCA and NiO, respectively. (b) The Ni–L edge from NCA and NiO standards taken under the same conditions. In NCA, the shift in L edge to higher energy is due to higher Ni valence (Ni^{3+}) as compared to NiO (Ni^{2+}). (c) Low energy loss region, showing Ni–M and Li–K for NCA and Ni–M for NiO. (d) Low energy loss region, showing Ni–M and Li–K for NCA in delithiated (Blue) and lithiated (Red) samples. The residual peak of the delithiated sample could be attributed to the Co–M edge.

We have followed particularly the evolution of the O–K near edge structure. In NCA, the oxygen K-edge consists of two peaks as shown in Figure 8a. The main peak depicts the electron energy loss due to the transition from core level ($1s$) to vacuum while the oxygen pre-edge peak reveals subtle structure/bonding characteristics caused by a transition from core O $1s$ to hybridized O $2p$ -Ni $3d$ orbitals.⁶² Changes in position (ΔE) and intensity of the oxygen pre-edge peak with respect to the main peak ($I_{\text{pre}}/I_{\text{Main}}$) show the local coordination environment between transition metals and

oxygen. The core loss spectra for all samples in this study were calibrated using the O–K main peak at 538 eV. Pristine NCA has a ΔE of 12.5 eV while it reduces to 8 eV for NiO. In NiO, the prepeak is lower in intensity than in NCA. The $(I_{\text{Pre}}/I_{\text{Main}})$ intensity ratios for pristine NCA and NiO are 0.46 and 0.38, respectively.

The Li–K and Ni–M edges are found near the plasmon loss region of the spectrum. The Li–K edge is situated at around 60 eV and the Ni–M edge is around 69 eV as shown in Figure 8c. For all low loss measurements in this study, the EELS spectra were calibrated using the Ni–M edge at 69 eV. In the low loss region, there is a superposition of Li–K, Co–M, and Ni–M edges and the corresponding spectrum is therefore complex as these edges partially overlap with each other and their position and intensity could shift due to changes in valence state.⁶³ The Li–K and Ni–M edges for lithiated and delithiated NCA are shown in Figure 8d and we have attributed the changes in peak intensity at around 62 eV to be due to the presence of Li. In this study, we have used the Li–K/Ni–M intensity ratio as a qualitative measure of the presence of Li in the structure. As the shape of the Li–K and Li–M edges are unknown, the Li–K and Ni–M edges were not deconvoluted. The Li–K/Ni–M intensity ratio provides only a qualitative measurement of Li content in the sample.

The other characteristic features of EELS are the L_2 and L_3 edges of transition metal M (M = Ni or Co) resulting from a transition from $2p_{1/2}$ or $2p_{3/2}$ states to unoccupied 3d states. Any reduction of a transition metal valence state can be measured qualitatively from a shift to the left of the L_3 peak position, and the valence states can be determined from the L_3/L_2 peak intensity ratio.^{64–67} Metal oxides with well-known valence states were used as standards for calibration purposes. Further details of valence measurements from standard oxides can be found elsewhere.^{66,67}

The EELS results presented here and the conclusions about the chemistry of surface phases drawn from them are based on measurements taken from several particles and surfaces. Although we have chosen suitable areas (thin sample within 10 nm from the edge and similar STEM contrast) for EELS measurements, there is an inevitable statistical variation in the results. While drawing the conclusions about the chemical nature of the surface phases, it was made sure that the measurements fall within a permitted statistical error. A table containing standard deviation and percentage error for all EELS data is shown in Supporting Information Table S1. Most EELS data are reported with less than 5% error except for the Li–K/Ni–M ratio which could exceed 15%. The largest error over 15% occurs for Co concentration and Li–K/Ni–M ratio determinations due to the low EELS signal and inaccuracy in background determination.

Quantitative measurements of four EELS parameters—(a) the oxygen prepeaks separation (ΔE) and the intensity ratio of O pre and main peaks ($I_{\text{Pre}}/I_{\text{Main}}$), (b) M/O concentration ratio (with M = Ni + Co), (c) valence state of Ni, and (d) Li (K) edge/Ni (M) edge intensity ratio—as a function of distance from the edge of the particle are shown in Figures 9 and 10 for layered and extended rocksalt structures, respectively. The original EELS spectra as a function of distance are presented in Supporting Information Figures S4 and S5.

For the layered structure shown in Figure 9a, the EELS measurements (Figure 9b–e) reveal a gradual phase transformation from the surface to the interior of the particle. The

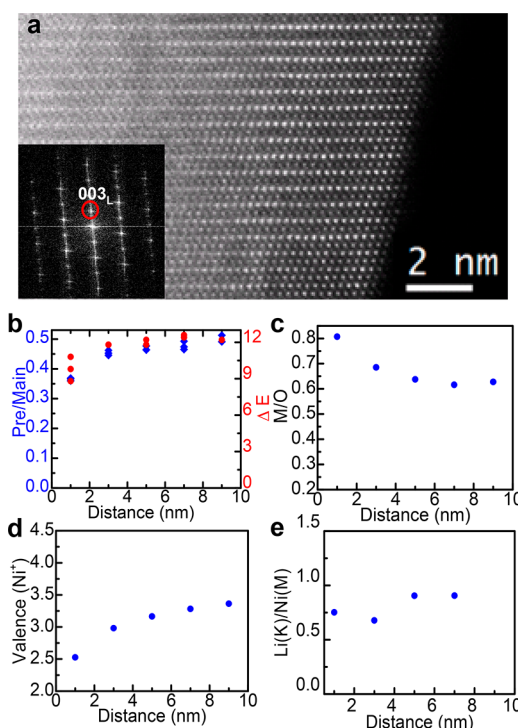


Figure 9. (a) HAADF STEM image and corresponding EELS measurements as a function of distance from the edge of the NCA cathode kept at constant voltage of 4.75 V for 2 weeks. The STEM contrast from this area is layered. The measured EELS parameters reveal a smooth change from the surface to the interior. At 1 nm from the surface, (b) the intensity ratio of the O K-edge pre and main peaks is 0.35, and the difference (ΔE) in the peak positions is 10 eV, (c) the M/O ratio is 0.8 (with M = Ni + Co), (d) Ni valence +2.5. (e) The Li(K)/Ni(M) concentration ratio increases from about 0.6 to 0.9.

ΔE value for O–K is increasing gradually from 8.5 and 12 eV, while $(I_{\text{Pre}}/I_{\text{Main}})$ increases from 0.32 to 0.5. The M/O ratio is 0.8, 1 nm from the surface with a Ni valence state converging to Ni^{2+} at the surface. All these core-loss parameters saturate slightly above 10 nm and converge to values corresponding to pristine NCA. The Li–K/Ni–M ratio is approximately 0.6 within the first 3 nm and jumps to 0.9 above this distance. The presence of Li in the surface region shows that Li has intercalated back into the structure. This also corroborates the electrochemical results (Table 1), which show that nearly 81% of the Li has reintercalated into the cathode after discharge to 2.7 V. A similar image contrast with chemical changes with a continuous transition from layer to rocksalt has been observed for NCA aged 2 weeks at 4.5 V (cf. Supporting Information Figure S6).

In contrast, the EELS results from the extended rocksalt contrast (cf. Figure 6b) reveal a totally different behavior as shown in Figure 10. First the oxygen prepeak is pronounced ($I_{\text{Pre}}/I_{\text{Main}} = 0.35$), with a $\Delta E = 11$ eV similar to values reported for spinel⁶⁸ with a high average $\text{Ni}^{3.5+}$ valence state. In order to confirm this result, we have looked at the O–K near edge structure for various cobalt oxides (Supporting Information Figure S7), and indeed the spinel cobalt oxide has a similar near edge structure as layered despite having one Co in the tetrahedral site. The oxygen prepeak position ΔE decreases from 11.5, 11.0, 10.3, and 7.0 eV for spinel $\text{Fm}\bar{3}\text{m}$ Co_3O_4 , layered $\text{R}\bar{3}\text{m}$ LiCoO_2 , trigonal $\text{R}\bar{3}\text{c}$ Co_2O_3 , and rocksalt

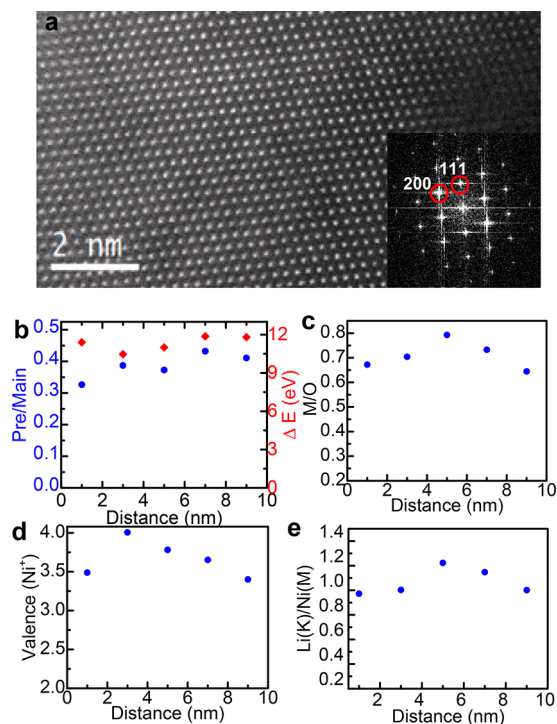


Figure 10. HAADF STEM image and corresponding EELS measurements as a function of distance from the surface of the NCA cathode kept at constant voltage at 4.75 V for 2 weeks. The STEM ADF contrast from the corresponding area reveals a rocksalt type structure. The EELS data are rather random with average values of (a) intensity ratio of O K-edge pre and main peaks of 0.4, and the difference (ΔE) in the peak positions of 11 eV, (b) M/O ratio ~ 0.7 (with M = Ni+Co), (c) Ni valence +3.6. (d) The Li concentration remains almost constant with Li(K)/Ni(M) ~ 1.1 .

$Fm\bar{3}m$ CoO, respectively. With a transition metal to oxygen ratio of 0.7, this extended rocksalt phase is considerably reduced as compared to $LiMO_2$ or spinel LiM_2O_4 with an M/O ratio of 0.5. The Li content in this extended rocksalt phase is higher compared to that of the layered phase. In addition, the scattered nature of the measured EELS parameters which exceed the data accuracy (cf. Table S1) shows that this phase is chemically very inhomogeneous, consistent with the intensity variations observed by HAADF-STEM imaging (See Figure 6d). Although this phase has the $Fm\bar{3}m$ space group as revealed by FFT from HAADF-STEM images, the corresponding EELS results point toward a phase chemically resembling more of a disordered spinel or disordered layered phase.

In this study, we have not observed any significant variation in the energy position of the Co- L_3 edge from the interior to the surface, implying that Co remains in a Co^{3+} valence state in agreement with earlier XAS experiments on NCA.⁶⁹ However, other investigations by STEM/EELS²³ and XAS,⁷⁰ also on NCA, do report a reduction of Co at the surface. Historically, Co was added to nickel-based layered oxide in order to increase its stability against oxygen loss and phase changes. This apparent discrepancy between these studies could be due to the increased stability induced by Co and to local variation in chemistry between samples.

3.3. Surface Phase Evolution at 4.75 V and 60 °C. The NCA cathodes were also subjected to constant voltage aging at a high temperature of 60 °C under the same voltages of 4.1, 4.5, and 4.75 V. The electrochemical degradation was analyzed

by combined impedance spectroscopy and microcalorimetry measurements.⁵⁰ For 4.1 and 4.5 V, no change in current could be measured with an observed microstructure similar to that observed at RT with rocksalt contrast at the surface and spinel type reflections further in the interior (cf. Supporting Information Figure S8). At 4.75 V however, a sharp increase in current is measured peaking at about 80–90 h which is due in part to an exothermic reaction within the cell. In these conditions, the impedance is so high that subsequent lithiation at lower voltage is not occurring. Further details of high temperature electrochemical behavior in $LiPF_6$ and $LiBF_4$ electrolytes are presented in a companion paper.⁵⁰

During high temperature aging at 4.75 V, the characteristic morphological/crystallographic features before and after exothermic reaction show drastic changes. The pre-exothermic samples have similar features as that of the RT samples at 4.75 V (cf. Supporting Information Figure S9). In the post-exothermic samples, extensive surface morphological and structural changes were observed. On some surfaces, we have observed a high level of surface porosity as shown in Figure 11.

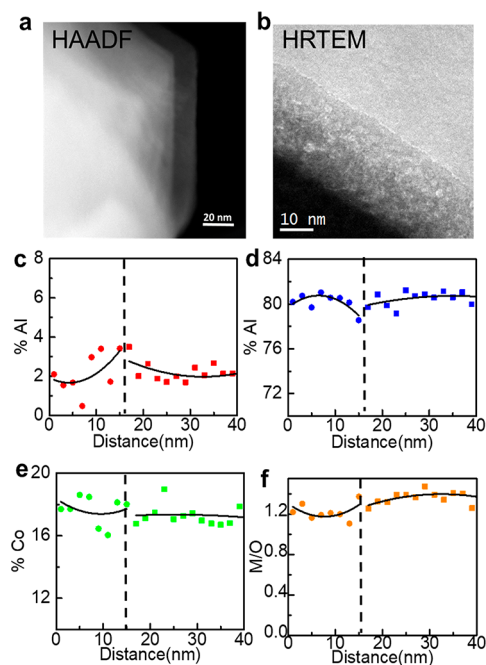


Figure 11. (a) HAADF-STEM image and (b) HRTEM image of NCA cathode held at constant voltage of 4.75 V and at 60 °C revealing surface porosity with corresponding X-ray EDS intensity profile across the interface for (c) Al, (d) Ni, and (e) Co. In part (f), the M in the M/O ratio represents Ni+Co+Al.

The low magnification HAADF-STEM image shows a darker surface contrast indicative of a surface region with lower density while the corresponding TEM image (cf. Figure 11b) taken at a small defocus value reveals pores 1–3 nm in diameter. The extent of this porous surface layer varies between 10 and 20 nm in thickness. The corresponding X-ray EDS analysis, shown in Figure 11c–f, reveals a composition for this porous surface layer which is comparable to that of the bulk interior. The 2–3% Al content in the surface layer is lower than the value of 5–6% measured for as synthesized NCA powder (cf. Supporting Information Figure S10). Besides extensive surface porosity, we also observe the appearance of more rugged surfaces as shown in Figure 12b and 12d. We also

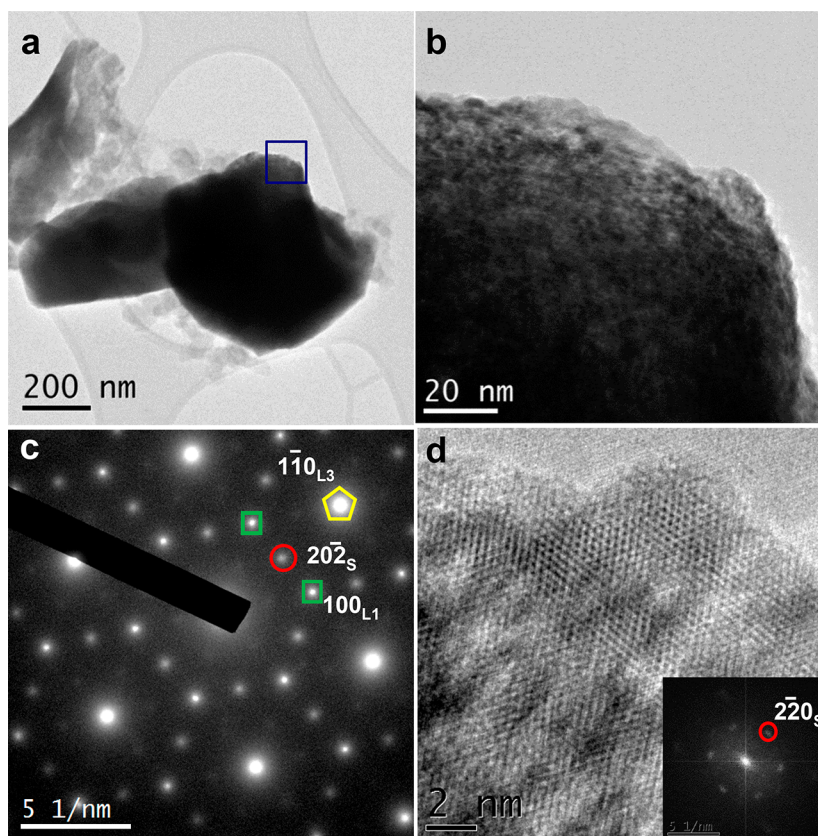


Figure 12. (a) Low magnification NCA particle after aging for 150 h at 4.75 V and 60 °C (after exothermic reaction) with (b) higher magnification images showing severely corroded surfaces (c). The selected area diffraction shows a complex pattern formed by the coexistence of three phases corresponding to O3 ($R\bar{3}m$), spinel ($Fd\bar{3}m$), and O1 ($P\bar{3}m1$) phases. The spots for O3 and O1 phases are marked as L_3 (pentagon) and L_1 (square), respectively (See Supporting Information Figure S12 for indexing). (d) HRTEM image and corresponding FFT reveal mostly spinel phase at the surface ($[001]_R$ zone axis).

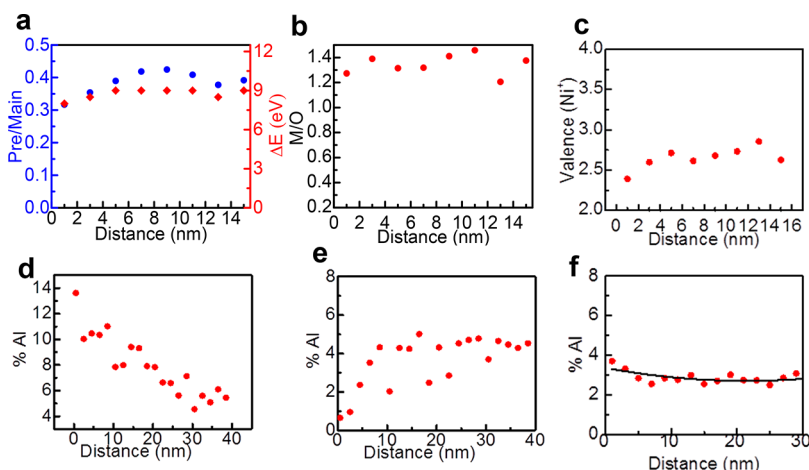


Figure 13. EELS data profile for NCA aged 150 h at 4.75 V and 60 °C revealing a heavily reduced surface region with (a) low average ΔE of 8.5 eV and O–K pre/main peak of 0.35–0.4, (b) an average high M/O ratio of 1.3 (with M = Ni+Co) and (f) low average Ni valence of about $Ni^{+2.5}$. Corresponding X-ray EDS Al concentration profiles (at%) revealing (d) Al surface enrichment and (e) Al surface depletion within (f) average Al concentration profile taken from 8 particles.

attribute the increase in surface roughness and surface porosity to metal dissolution from the cathode with possibly migration to the anode. Anode plating has indeed been detected directly by X-ray EDS spectroscopy with the cell impedance drastically reduced upon substitution with a new anode⁵⁰ (cf. Supporting Information Figure S11). The diffraction pattern obtained from the near surface region revealed the presence of layered

and spinel reflections. In some areas, a more complex diffraction pattern is observed revealing the presence of the O1 phase ($P\bar{3}m1$) in addition to spinel and layered phases as shown in Figure 12c. The FFT from the corresponding HRTEM image also shows spinel type reflections and structure. For detailed indexing of the diffraction pattern see the Supporting Information (Supporting Information Figure

S12). This O1 phase is not commonly observed in NCA⁸ because the presence of 5% Al prevents complete delithiation, but the O1 phase has been found to be thermodynamically stable in delithiated LiNiO₂.⁸ Additionally, the O1 phase has been observed in another TEM investigation for NMC333 (LiNi_{0.33}Mn_{0.33}Co_{0.33}O₂) cathode in an overcharged highly delithiated state.²⁶

The oxygen fine structure and Ni valence state of this transformed surface have been measured by EELS (cf. Figure 13) along with X-ray EDS for Al concentration profiles determination. From the EELS measurement depicted in Figure 13a–c, it appears that the surface is heavily reduced with high oxygen loss. The average values within the first 15 nm for O–K edge are approximately $\Delta E = 8.5$ eV and $I_{(\text{Pre}/\text{Main})} = 0.35$, values which are close to what is measured for the standard NiO (cf. Figure 8). The average Ni⁺ valence state of +2.5 is also low, revealing mixed Ni²⁺ and Ni³⁺ valence state. Surprisingly, the M/O ratio (with M = Ni+Co) from post exothermic reaction samples is always >1, implying that there is Ni and Co enrichment at the surface. These surface enrichment measurements obtained by EELS are consistent with the results obtained by X-ray EDS for the porous surface (cf. Figure 11). There are two possible ion migration paths subsequent to metal dissolution from the surface: (i) migrate to the anode or¹¹ redeposition onto the cathode surface in the form of metal fluoride or other metal compounds. A redeposition process into nonoxide compounds could explain the increased M/O ratio measured on the cathode surface. Besides redeposition onto the cathode, migration to the anode is also occurring as Ni and Co in metallic form has been detected on the anode by EDS and X-ray diffraction measurements.⁵⁰ Additional EELS measurements from the Li–K and Ni–M region show that the surface has a negligible amount of lithium, which is consistent with the electrochemistry results in which the impedance becomes too high and the cell could not be discharged; that is, Li did not intercalate back into the cathode (Table 1). The Al X-ray EDS concentration profiles for various surfaces are depicted in Figure 13d–f. Two extreme cases of Al surface enrichment and Al depletion are shown in Figure 13d and 13e, respectively, with the average Al concentration from eight surfaces shown in Figure 13f. As measured on the porous surface (cf. Figure 11) the average Al content of 3% is lower than the value of 5–6% measured on the as synthesized NCA (cf. Supporting Information Figure S10). Although a relatively high Al content is at this time measured, we have not observed any AlO_x surface layer. We also observe a large variation in chemistry from particle to particle which indicates that dissolution is not occurring uniformly, but on average, all elements, Al, Co, and Ni appear to dissolve from the surface in equal proportion.

4. DISCUSSION

In this investigation, four major new results are reported:

- A thin rocksalt phase with low valence state is always observed at the particle surfaces for all voltages with a smooth solid solution type transition to interior layered structure. This surface phase transformation is driven by surface oxygen losses.
- A second extended rocksalt phase with high valence state and oxygen K-edge characteristic of layered or spinel Li_xMO₂ is also observed but predominantly at 4.75 V.

- Although surface structural changes and metal dissolution are both important degradation mechanisms inducing an impedance rise, metal dissolution is the dominant mechanism at 4.75 V and 60 °C leading to reduced and porous surface layers.

- Occasional appearance of a near surface O1 phase for NCA cathodes held at 4.75 V and 60 °C which become thermodynamically stable from local Al depletion from the surface.

Under high constant voltage aging, the crystal structure and chemistry of the surface of NCA particles show a transformed surface consisting of thin (1–2 nm) rocksalt surface phase at all conditions including on the pristine material, with intermediate spinel type reflections prominent after charging to 4.5 V. The presence of spinel type reflections is less prominent at 4.75 V, but instead an extended phase with rocksalt structure is observed. In this study, we observed two types of rocksalt phases having different chemical characteristics as determined by EELS. In the first case, the overall HAADF-STEM image contrast is mostly layered (See Figure 5a) with increasing occupation of the Li 3b site with M ions (M = Ni, Co, and Al) with the rocksalt contrast confined within the first few atomic layers from the surface. The average Ni valence from this 1 nm surface rocksalt region is +2.5 with an M/O ratio of 0.8. For this first rocksalt phase, the oxygen k-edge prepeak, Ni valence, and M/O ratio as well as quantitative HAADF-STEM image contrast, with migration of M to Li 3b site, reveal a gradual continuous change from layered to rocksalt. The extent of this gradual phase change varies from particle to particle and ranges from about 5 nm to over 20 nm with a tendency to increase with increasing voltage (cf. Figure 7). Therefore, the layered structure and the rocksalt phase appear to form a complete solid solution without any abrupt interface. Such continuous phase change from layered to rocksalt occurs with a gradual decrease in M/O ratio.

For the second phase with extended rock salt contrast (cf. Figures 6 and 10) there is no gradual variation in contrast or chemistry from interior to surface, but a random behavior is shown over large distances exceeding 20 nm. The average Ni valence value of +3.6 is much higher than for the rocksalt surface and also has a much larger oxygen prepeak position of 11.5 eV and an average M/O of 0.7. The Li content of this extended rocksalt phase is also larger than for the thin surface rocksalt phase. This rocksalt contrast has oxygen EELS characteristics of a cation disordered reduced spinel phase (Li_xM₂^{+3.6}O_{4-x}) with Fm $\bar{3}$ m space group symmetry.

An important point to note here is that the two rocksalt phases with Fm $\bar{3}$ m space group can have a wide range of crystal chemistries containing Li, Al, with general composition Li_xMO_y, (M = Ni, Co, Al). These phases can be described as transition metal disordered phases with rocksalt Fm $\bar{3}$ m space group symmetry. The presence of a rocksalt structure with random occupation of M in the Li layer has been reported extensively in the literature^{71–73} and has been described as both defect-spinel⁴⁴ or disordered rocksalt.^{74,75} In our study, the presence of a dense rocksalt phase M⁺²O (M = Ni, Co) has not been observed for any of the surface phases as both Li and Al are present at the surface. In addition the HAADF contrast variations reveal that these phases have considerable amount of metal vacancies. After discharge, Li is measured within these phases, indicative that Li transport has occurred through these rocksalt phases. Recent studies on Li transport in disordered

rocksalt phases by G Ceders's group⁴⁸ show that within a range of Li excess, Li transport in cubic phases is indeed possible via a percolation pathway. They also showed that cation disorder is not necessarily detrimental for layered structures as long as there is a sufficient amount of excess Li in the composition. Also, the presence of transition metal and oxygen vacancies may increase the Li concentration range allowing Li diffusion through the rocksalt and disordered layered phases. Although layered structures have a higher intrinsic Li diffusivity than disordered rocksalt,⁴⁸ Li transport is still occurring and the large impedance rise measured at 4.75 V cannot be attributed uniquely to surface structural changes, and reactions with the electrolyte leading to the formation of surface layer on the cathode may play the most significant role.

One important results of this study is the measurement of oxygen loss associated with surface phase transformations. Oxygen loss during surface phase transformation is a complex process caused by at least two possible simultaneous processes. First, oxygen loss at high delithiation ($\text{Li} < 0.15$) has been reported previously in Ni-rich layered oxide.³¹ At the highly delithiated state, Ni^{3+} oxidizes to Ni^{4+} which is accompanied by removal of an electron from the t2g band. Since, the t2g band overlaps with the O 2p band, electrons would be removed from the O 2p band as well as creating holes or oxygen vacancies. In the case of NCA t2g lies deep within the O 2p band, so that higher amounts of delithiation are needed to initiate this process.⁷⁶ Second, the electrolyte plays a very significant role in oxygen loss from the surface.⁵⁰ At high voltage and high temperature a reducing environment is formed at the cathode–electrolyte interface which causes the release of more oxygen with a concomitant decrease in Ni valence state from Ni^{4+} to Ni^{2+} .

The O1 phase is not commonly observed in NCA as it is generally argued that this O1 phase is thermodynamically stable only in the fully delithiated state.⁸ In NCA, because of the presence of electrochemically inactive 5% Al which remains as Al^{3+} , there is therefore 5% residual Li making the O1 phase less thermodynamically stable than the O3 phase. However, because of the observed preferential and inhomogeneous metal dissolution, the Al content at the surface could be in some areas as low as 2% or even less (see Figures 11c and 13e) and with an undetectable Li surface content as measured by EELS. In these surface areas, with low Al and Li content, the O1 phase could therefore become thermodynamically stable as observed experimentally.

The (Ni–Li–Vacancy)O ternary phase diagram was recently computed at 600 K using first-principle simulation based techniques.⁷⁷ In addition to the known LiNiO_2 , NiO_2 , NiO , and spinel LiNi_2O_4 phases, they predicted the existence of three new phases along the oxygen loss path between NiO_2 and NiO . These phase are $\beta\text{-Ni}_{1.25}\text{O}_2$ ($R\bar{3}m$), $\gamma\text{-Ni}_{1.50}\text{O}_2$ ($Cmmm$), and $\delta\text{-Ni}_{1.75}\text{O}_2$ ($Fm\bar{3}m$). One common feature in these three phases is the gradual filling of the vacant Li layer with ordering of vacancy and Ni ion on alternate Li vacant sites. This periodic ordering which is similar to the Ni periodic arrangement in the spinel phase (See Figure 3b) gives rise to extra reflections which are qualitatively identical to extra reflections in the LiNi_2O_4 spinel phase. In this study we indexed the diffraction pattern and FFT of Figure 12c and S8 with standard spinel reflection. However, in view of the limited extended solubility of the spinel LiNi_2O_4 phase⁷⁷ it is unlikely that the observed surface phase, which is heavily reduced with low Ni valence state of about $\text{Ni}^{2.5}$, is actually spinel and could

actually be the $\delta\text{-Ni}_{1.75}\text{O}_2$ phase. The simulated diffraction pattern along the $[111]$ zone axis of $\delta\text{-Ni}_{1.75}\text{O}_2$ ($Fm\bar{3}m$) with lattice parameter $a = 0.835$ nm gives rise to a diffraction pattern which is qualitatively similar to that of LiNi_2O_4 spinel. Only quantitative analysis of diffracted intensities or of HAADF-STEM images would provide a unique identification of these phases.

5. CONCLUSION

The surface chemical and structural evolution of electrochemically stressed NCA layered cathode under extreme voltage up to 4.75 V and temperature of 60 °C conditions were studied using high resolution TEM, STEM, EELS, and EDS. A large impedance rise is observed at 4.75 V and RT which is due primarily to surface structural changes which follows the layered to rocksalt phase transformation scheme. Quantitative STEM/EELS chemical and valence analysis reveal a continuous solid solution type transformation from layered to rocksalt phase. A second type of extended image contrast with rocksalt crystal structure has been observed. The corresponding EELS data reveal a chemistry and valence state similar to an oxygen reduced disordered spinel-like phase. These phase transformations have been facilitated by reactions with the electrolyte leading to surface oxygen loss and movement of cations from its original transition metal 3a position to the Li 3b position. After discharge, Li has been detected indicating that Li transport has occurred through these rocksalt phases. At 60 °C and 4.75 V microstructural changes are dominated by extensive metal dissolution from the cathode. This dissolution process leads to the formation of a highly reduced and porous surface layer with in some areas denuded of Al. These low Al regions lead to complete delithiation and allow a phase transition to the O1 phase with space group $P\bar{3}m1$.

■ ASSOCIATED CONTENT

📄 Supporting Information

The Supporting Information is available free of charge on the ACS Publications website at DOI: 10.1021/acs.chemmater.7b05305.

Selected area diffraction, high-resolution images, simulation of HAADF images, EDS measurements, and EELS measurements of some of the phases (PDF)

■ AUTHOR INFORMATION

Corresponding Author

*E-mail: grad.pinaki@gmail.com; cosandey@rutgers.edu. Now at Michigan Technological University, 1400 Townsend Drive, Houghton, MI-49931.

ORCID

Pinaki Mukherjee: 0000-0001-9428-8428
Nicholas V. Faenza: 0000-0002-2620-4592
Louis F. J. Piper: 0000-0002-3421-3210
Glenn G. Amatucci: 0000-0003-1905-6197

Notes

The authors declare no competing financial interest.

■ ACKNOWLEDGMENTS

The authors thank Hena Das and Gerbrand Ceder for useful discussions on phase transformation. At BLN-CFN we thank Dong Su for his help on STEM/EELS during the early phase of this research and Huolin Xin for his help with STEM/EDS

analysis. This material is based upon work supported as part of NECCES, an Energy Frontier Research Center funded by the U.S. Department of Energy, Office of Basic Energy Sciences under Award Number DE-SC0012583. This research used resources of the Center for Functional Nanomaterials, which is a U.S. DOE Office of Science Facility, at Brookhaven National Laboratory under Contract No. DE-SC0012704. Work at the Molecular Foundry was supported by the Office of Science, Office of Basic Energy Sciences, of the U.S. Department of Energy under Contract No. DE-AC02-05CH11231. A part of the electron microscopy research was performed at the Applied Chemical and Morphological Analysis Laboratory (ACMAL) at Michigan Technological University. The ACMAL electron microscopy facility is supported by NSF MRI 1429232.

REFERENCES

- (1) Whittingham, M. S. Lithium Batteries and Cathode Materials. *Chem. Rev.* **2004**, *104*, 4271–4301.
- (2) Erickson, E. M.; Ghanty, C.; Aurbach, D. New Horizons for Conventional Lithium Ion Battery Technology. *J. Phys. Chem. Lett.* **2014**, *5*, 3313–3324.
- (3) Ellis, B. L.; Lee, K. T.; Nazar, L. F. Positive Electrode Materials for Li-Ion and Li-Batteries. *Chem. Mater.* **2010**, *22*, 691–714.
- (4) Rozier, P.; Tarascon, J. M. Review—Li-Rich Layered Oxide Cathodes for Next-Generation Li-Ion Batteries: Chances and Challenges. *J. Electrochem. Soc.* **2015**, *162* (14), A2490–A2499.
- (5) Jain, A.; Ong, S. P.; Hautier, G.; Chen, W.; Richards, W. D.; Dacek, S.; Cholia, S.; Gunter, D.; Skinner, D.; Ceder, G.; Persson, K. A. Commentary: The Materials Project: A Materials Genome Approach to Accelerating Materials Innovation. *APL Mater.* **2013**, *1*, 011002.
- (6) Nitta, N.; Wu, F.; Lee, J. T.; Yushin, G. Li-Ion Battery Materials: Present and Future. *Mater. Mater. Today* **2015**, *18*, 252–264.
- (7) Robert, R.; Villeville, C.; Novak, P. Enhancement of the High Potential Specific Charge in Layered Electrode Materials for Lithium-Ion Batteries. *J. Mater. Chem. A* **2014**, *2*, 8589–8598.
- (8) Radin, M.; Hy, S.; Sina, M.; Fang, C.; Liu, H.; Vinckeviciute, J.; Zhang, H.; Whittingham, M. S.; Meng, Y. S.; Van der Ven, A. Narrowing the Gap Between Theoretical and Practical Capacities in Layered Li-Ion Cathode Materials. *Adv. Energy Mater.* **2017**, *7*, 1602888.
- (9) Vetter, J.; Novak, P.; Wagner, M. R.; Veit, C.; Müller, K. C.; Besenhard, J. O.; Winter, M.; Wohlfahrt-Mehrens, M.; Vogler, C.; Hammouche, A. Ageing Mechanisms in Lithium-Ion Batteries. *J. Power Sources* **2005**, *147*, 269–281.
- (10) Hausbrand, R.; Cherkashinin, G.; Ehrenberg, H.; Groting, M.; Albe, K. Fundamental Degradation Mechanisms of Layered Oxide Li-Ion Battery Cathode Materials: Methodology, Insight and Novel Approaches. *Mater. Sci. Eng., B* **2015**, *192*, 3–25.
- (11) Mohanty, D.; Li, J.; Nagpure, S. C.; Wood, D. L., III; Daniel, C. Understanding the Structure and Structural Degradation Mechanisms in High-Voltage, Lithium-Manganese-Rich Lithium-Ion Battery Cathode Oxide: A Review of Materials Diagnostics. *MRS Energy & Sustainability* **2015**, *2* (e15), 1–24.
- (12) Xu, J.; Lin, F.; Doeff, M. M.; Tong, W. A Review of Ni-Based Layered Oxides for Rechargeable Li-Ion Batteries. *J. Mater. Chem. A* **2017**, *5*, 874–901.
- (13) Liu, W.; Oh, P.; Liu, X.; Lee, M.-J.; Cho, W.; Chae, S.; Kim, Y.; Cho, J. Nickel-rich Layered Lithium Transition-Metal Oxide for High-Energy Lithium-Ion Batteries. *Angew. Chem., Int. Ed.* **2015**, *54*, 4440–4457.
- (14) Itou, Y.; Ukyo, Y. Performance of LiNiCoO₂ Materials for Advanced Lithium-Ion Batteries. *J. Power Sources* **2005**, *146*, 39–44.
- (15) Watanabe, S.; Kinoshita, M.; Hosokawa, T.; Morigaki, K.; Nakura, K. Capacity Fade of LiAl_xNi_{1-x-y}Co_yO₂ Cathode for Lithium-Ion Batteries During Accelerated Calendar and Cycle Life Tests (Surface Analysis of LiAl_xNi_{1-x-y}Co_yO₂ Cathode after Cycle Tests in Restricted Depth of Discharge Ranges). *J. Power Sources* **2014**, *258*, 210–217.
- (16) Yan, P.; Zheng, J.-C.; Gu, M.; Xiao, J.; Zhang, H.; Wang, C.-M. Intragranular Cracking as a Critical Barrier for High-Voltage Usage of Layer-Structured Cathode for Lithium-Ion Batteries. *Nat. Commun.* **2017**, *8*:14101 (Jan 16), 1–11.
- (17) Makimura, Y.; Zheng, S.; Ikuhara, Y.; Ukyo, Y. Microstructural Observation of LiNi_{0.8}Co_{0.15}Al_{0.05}O₂ after Charge and Discharge by Scanning Transmission Electron Microscopy. *J. Electrochem. Soc.* **2012**, *159*, A1070–A1073.
- (18) Arai, H. Thermal Behavior of Li_{1-y}NiO₂ and the Decomposition Mechanism. *Solid State Ionics* **1998**, *109*, 295–302.
- (19) Sasaki, T.; Nonaka, T.; Oka, H.; Okuda, C.; Itou, Y.; Kondo, Y.; Takeuchi, Y.; Ukyo, Y.; Tatsumi, K.; Muto, S. Capacity-Fading Mechanisms of LiNiO₂-Based Lithium-Ion Batteries. *J. Electrochem. Soc.* **2009**, *156* (4), A289–A293.
- (20) Choi, W.; Manthiram, A. Comparison of Metal Ion Dissolution from Lithium Ion Battery Cathode. *J. Electrochem. Soc.* **2006**, *153* (9), A1760–A1764.
- (21) Wandt, J.; Freiberg, A.; Thomas, R.; Gorlin, Y.; Siebel, A.; Jung, R.; Gasteiger, H. A.; Tromp, M. Transition Metal Dissolution and Deposition in Li-Ion Batteries Investigated by Operando X-Ray Absorption Spectroscopy. *J. Mater. Chem. A* **2016**, *4*, 18300–18305.
- (22) Pieczonka, N. P. W.; Liu, Z.; Lu, P.; Olson, K.; Moote, J.; Powell, B. R.; Kim, J.-H. Understanding Transition-Metal Dissolution Behavior in LiNi_{0.3}Mn_{1.5}O₄ High-Voltage Spinel for Lithium Ion Batteries. *J. Phys. Chem. C* **2013**, *117*, 15947–15957.
- (23) Zheng, S.; Huang, R.; Makimura, Y.; Ukyo, Y.; Fisher, C. a. J.; Hirayama, T.; Ikuhara, Y. Microstructural Changes in Li-Ni_{0.8}Co_{0.15}Al_{0.05}O₂ Positive Electrode Material During the First Cycle. *J. Electrochem. Soc.* **2011**, *158* (4), A357–362.
- (24) Guilnard, M.; Croguennec, L.; Delmas, C. Thermal Stability of Lithium Nickel Oxide Derivatives. Part II. *Chem. Mater.* **2003**, *15*, 4484–4493.
- (25) Hwang, S.; Kim, S. M.; Bak, S.-M.; Cho, B.-W.; Chung, K. Y.; Lee, J. Y.; Chang, W.; Stach, E. Investigating Local Degradation and Thermal Stability of Charged Nickel-Based Cathode Materials through Real-Time Electron Microscopy. *ACS Appl. Mater. Interfaces* **2014**, *6*, 15140–15147.
- (26) Wu, L.; Nam, K.-W.; Wang, X.; Zhou, Y.; Zheng, J.-C.; Yang, X.-Q.; Zhu, Y. Structural Origin of Overcharge-Induced Thermal Instability of Ni-Containing Layered Cathodes for High-Energy-Density Lithium Batteries. *Chem. Mater.* **2011**, *23*, 3953–3960.
- (27) Bak, S.-M.; Nam, K.-W.; Chang, W.; Yu, X.; Hu, E.; Hwang, S.; Stach, E. a.; Kim, K.-B.; Chung, K. Y.; Yang, X.-Q. Correlating Structural Changes and Gas Evolution during the Thermal Decomposition of Charged Li_{1-x}Ni_{0.8}Co_{0.15}Al_{0.05}O₂ Cathode Materials. *Chem. Mater.* **2013**, *25*, 337–351.
- (28) Reed, J.; Ceder, G.; Van Der Ven, A. Layered-to-Spinel Phase Transition in Li_xMnO₂. *Electrochem. Solid-State Lett.* **2001**, *4*, A78–A81.
- (29) Xu, B.; Fell, C. R.; Chi, M.; Meng, Y. S. Identifying Surface Structural Changes in Layered Li-Excess Nickel Manganese Oxides in High Voltage Lithium Ion Batteries: A Joint Experimental and Theoretical Study. *Energy Environ. Sci.* **2011**, *4*, 2223–2233.
- (30) Chebiam, R. V.; Prado, F.; Manthiram, A. Soft Chemistry Synthesis and Characterization of Layered Li_{1-x}Ni_{1-y}Co_yO_{2-δ} (0 ≤ x ≤ 1 and 0 ≤ y ≤ 1). *Chem. Mater.* **2001**, *13*, 2951–2957.
- (31) Venkatraman, S.; Shin, Y.; A, M. Phase Relationships and Structural and Chemical Stabilities of Charged Li_{1-x}CoO_{2-δ} and Li_{1-x}Ni_{0.85}Co_{0.15}O_{2-δ} Cathodes. *Electrochem. Solid-State Lett.* **2003**, *6* (1), A9–A12.
- (32) Gabrisch, H.; Ozawa, Y.; Yazami, R. Crystal Structure Studies of Thermally Aged LiCoO₂ and LiMn₂O₄ Cathodes. *Electrochim. Acta* **2006**, *52*, 1499–1506.
- (33) Qian, D.; Xu, B.; Chi, M.; Meng, Y. S. Uncovering the Roles of Oxygen Vacancies in Cation Migration in Lithium Excess Layered Oxides. *Phys. Chem. Chem. Phys.* **2014**, *16*, 14665–14668.

- (34) Jiang, M.; Key, B.; Meng, Y. S.; Grey, C. P. Electrochemical and Structural Study of the layered, "Li-excess" Lithium-Ion Battery Electrode Material $\text{Li}[\text{Li}_{1/9}\text{Ni}_{1/3}\text{Mn}_{5/9}]\text{O}_2$. *Chem. Mater.* **2009**, *21*, 2733–2745.
- (35) Xu, B.; Qian, D.; Wang, Z.; Meng, Y. S. Recent Progress in Cathode Materials Research for Advanced Lithium Ion Batteries. *Mater. Sci. Eng., R* **2012**, *73*, 51–65.
- (36) Wang, L.; Maxisch, T.; Ceder, G. A First-Principles Approach to Studying the Thermal Stability of Oxide Cathode Materials. *Chem. Mater.* **2007**, *19*, 543–552.
- (37) Guilnard, M.; Croguennec, L.; Denux, D.; Delmas, C. Thermal Stability of Lithium Nickel Oxide Derivatives. Part I: $\text{Li}_x\text{Ni}_{1-0.2x}\text{O}_2$ and $\text{Li}_x\text{Ni}_{0.89}\text{Al}_{0.16}\text{O}_2$ ($x = 0.50$ and 0.30). *Chem. Mater.* **2003**, *15*, 4476–4483.
- (38) Yoon, W.-S.; Haas, O.; Muhammad, S.; Kim, H.; Lee, W.; Kim, D.; Fischer, D. A.; Jaye, C.; Yang, X.-Q.; Balasubramanian, M.; Nam, K.-W. In Situ Soft XAS Study of Nickel-Based Layered Cathode Material at Elevated Temperatures: A Novel Approach to Study Thermal Stability. *Sci. Rep.* **2015**, *4*:6827, 1–5.
- (39) Nam, K.-W.; Bak, S.-M.; Hu, E.; Yu, X.; Zhou, Y.; Wang, X.; Wu, L.; Zhu, Y.; K-Y, C.; Yang, X.-Q. Combining In-Situ Synchrotron X-Ray Diffraction and Absorption Techniques with Transmission Electron Microscopy to Study the Origin of Thermal Stability in Overcharged Cathode Materials for Lithium-Ion Batteries. *Adv. Funct. Mater.* **2013**, *23*, 1047–1063.
- (40) Qian, D.; Xu, B.; Chi, M.; Meng, Y. S. Uncovering the Roles of Oxygen Vacancies in Cation Migration in Lithium Excess Layered Oxides. *Phys. Chem. Chem. Phys.* **2014**, *16*, 14665–8.
- (41) Kim, G. Y.; Dahn, J. R. ARC Studies of the Effects of Electrolyte Additives on the Reactivity of Delithiated $\text{Li}_{1-x}[\text{Ni}_{1/3}\text{Mn}_{1/3}\text{Co}_{1/3}]\text{O}_2$ and $\text{Li}_{1-x}[\text{Ni}_{0.8}\text{Co}_{0.15}\text{Al}_{0.05}]\text{O}_2$ Positive Electrode Materials with Electrolyte. *J. Electrochem. Soc.* **2014**, *161* (9), A1394–A1398.
- (42) Täubert, C.; Fleischhammer, M.; Wohlfahrt-Mehrens, M.; Wietelmann, U.; Buhrmester, T. LiBOB as Electrolyte Salt or Additive for Lithium-Ion Batteries Based on $\text{LiNi}_{0.8}\text{Co}_{0.15}\text{Al}_{0.05}\text{O}_2$ /Graphite. *J. Electrochem. Soc.* **2010**, *157* (6), A721–A728.
- (43) Muto, S.; Sasano, Y.; Tatsumi, K.; Sasaki, T.; Horibuchi, K.; Takeuchi, Y.; Y, U. Capacity-Fading Mechanisms of LiNiO_2 -Based Lithium-Ion Batteries. *J. Electrochem. Soc.* **2009**, *156* (5), A371–A377.
- (44) Xu, B.; Fell, C. R.; Chi, M.; Meng, Y. S. Identifying Surface Structural Changes in Layered Li-Excess Nickel Manganese Oxides in High Voltage Lithium Ion Batteries: A Joint Experimental and Theoretical Study. *Energy Environ. Sci.* **2011**, *4*, 2223–2233.
- (45) Lin, F.; Markus, I. M.; Nordlund, D.; Weng, T.-C.; Asta, M.; Xin, H. L.; Doeff, M. M. Surface Reconstruction and Chemical Evolution of Stoichiometric Layered Cathode Materials for Lithium-Ion Batteries. *Nat. Commun.* **2014**, *5*, 3529.
- (46) Gao, P.; Ishikawa, R.; Tochigi, E.; Kumamoto, A.; Shibata, N.; Ikuhara, Y. Atomic-Scale Tracking of a Phase Transition from Spinel to Rocksalt in Lithium Manganese Oxide. *Chem. Mater.* **2017**, *29*, 1006–1013.
- (47) Lu, P.; Yan, P.; Romero, E.; Spoerke, E. D.; Zhang, H.; Wang, C.-M. Observation of Electron-Beam-Induced Phase Evolution Mimicking the Effect of the Charge–Discharge Cycle in Li-Rich Layered Cathode Materials Used for Li Ion Batteries. *Chem. Mater.* **2015**, *27*, 1375–1380.
- (48) Urban, A.; Lee, J.; Ceder, G. The Configurational Space of Rocksalt-Type Oxides for High-Capacity Lithium Battery Electrodes. *Adv. Energy Mater.* **2014**, *4* (13), 1400478.
- (49) Chen, C. H.; Liu, J.; Stoll, M. E.; Henriksen, G.; Vissers, D. R.; Amine, K. Aluminum-Doped Lithium Nickel Cobalt Oxide Electrodes for High-Power Lithium-Ion Batteries. *J. Power Sources* **2004**, *128*, 278–285.
- (50) Faenza, N. V.; Lebens-Higgins, Z. W.; Mukherjee, P.; Sallis, S.; Pereira, N.; Badway, F.; Halajko, A.; Ceder, G.; Cosandey, F.; Piper, L.; Amatucci, G. G. Electrolyte Induced Surface Transformation and Transition Metal Dissolution of Fully Delithiated Layered Compounds. *Langmuir* **2017**, *33*, 9333–9353.
- (51) Tarascon, J. M.; Gozdz, A. S.; Schmutz, C.; Shokoohi, F.; Warren, P. C. Performance of Bellcore's Plastic Rechargeable Li-Ion Batteries. *Solid State Ionics* **1996**, *86–88*, 49–54.
- (52) Manickam, M.; Takata, M. Effect of Cathode Binder on Capacity Retention and Cycle Life in Transition Metal Phosphate of a Rechargeable Lithium Battery. *Electrochim. Acta* **2003**, *48*, 957–963.
- (53) Markevich, E.; Salitra, G.; Aurbach, D. Influence of the PVdF Binder on the Stability of LiCoO_2 Electrodes. *Electrochem. Commun.* **2005**, *7*, 1298–1304.
- (54) Zheng, H.; Yang, R.; Liu, G.; Song, X.; Battaglia, V. S. Cooperation Between Active Material, Polymeric Binder and Conductive Carbon Additive in Lithium Ion Battery Cathode. *J. Phys. Chem. C* **2012**, *116*, 4875–4882.
- (55) Ohzuku, T.; Ueda, A.; Nagayama, M.; Iwakoshi, Y.; Komori, H. Comparative Study of LiCoO_2 , $\text{LiNi}_{1/2}\text{Co}_{1/2}\text{O}_2$ and LiNiO_2 for 4 V Secondary Lithium Cells. *Electrochim. Acta* **1993**, *38* (9), 1159–1167.
- (56) Choi, S.; Manthiram, A. Factors Influencing the Layered to Spinel-like Phase Transition in Layered Oxide Cathodes. *J. Electrochem. Soc.* **2002**, *149* (9), A1157–A1163.
- (57) Fultz, B.; Howe, J. *Transmission Electron Microscopy and Diffractometry of Materials*; Springer International: 2013; Vol. Fourth ed.
- (58) Pennycook, S. J. Z-contrast STEM for Materials Science. *Ultramicroscopy* **1989**, *30*, 58–69.
- (59) Hartel, P.; Rose, H.; Dinges, C. Conditions and Reasons for Incoherent Imaging in STEM. *Ultramicroscopy* **1996**, *63*, 93–114.
- (60) Jarvis, K. A.; Wang, C.-C.; Manthiram, A.; Ferreira, P. J. The Role of Composition in the Atomic Structure, Oxygen Loss, and Capacity of Layered Li–Mn–Ni Oxide Cathodes. *J. Mater. Chem. A* **2014**, *2*, 1353–1361.
- (61) Jarvis, K. A.; Wang, C. C.; Knight, J. C.; Rabenberg, L.; Manthiram, A.; Ferreira, P. J. Formation and Effect of Orientation Domains in Layered Oxide Cathodes of Lithium-Ion Batteries. *Acta Mater.* **2016**, *108*, 264–270.
- (62) Graetz, J.; Ahn, C. C.; Yazami, R.; Fultz, B. An Electron Energy-Loss Spectrometry Study of Charge Compensation in $\text{LiNi}_{0.8}\text{Co}_{0.2}\text{O}_2$. *J. Phys. Chem. B* **2003**, *107*, 2887–2891.
- (63) van Aken, P. A.; Styrsa, V. J.; Liebscher, B.; Woodland, A. B.; Redhammer, G. J. Microanalysis of $\text{Fe}^{3+}/\Sigma\text{Fe}$ in Oxide and Silicate Minerals by Investigation of Electron Energy-Loss Near-Edge Structures (ELNES) at the Fe $M_{2,3}$ Edge. *Phys. Chem. Miner.* **1999**, *26*, 584–590.
- (64) Graetz, J.; Ahn, C. C.; Ouyang, H.; Rez, P.; Fultz, B. White Lines and d-Band Occupancy for the 3d Transition-Metal Oxides and Lithium Transition-Metal Oxides. *Phys. Rev. B: Condens. Matter Mater. Phys.* **2004**, *69*, 1–6.
- (65) Graetz, J.; Hightower, A.; Ahn, C. C.; Yazami, R.; Rez, P.; Fultz, B. Electronic Structure of Chemically-Delithiated LiCoO_2 Studied by Electron Energy-Loss Spectrometry. *J. Phys. Chem. B* **2002**, *106*, 1286–1289.
- (66) Cosandey, F.; Su, D.; Sina, M.; Pereira, N.; Amatucci, G. G. Fe Valence Determination and Li Elemental Distribution in Lithiated $\text{FeO}_{0.7}\text{F}_{1.3}/\text{C}$ Nanocomposite Battery Materials by Electron Energy Loss Spectroscopy (EELS). *Micron* **2012**, *43*, 22–29.
- (67) Wang, Z. L.; Yin, J. S.; Jiang, Y. D. EELS Analysis of Cation Valence States and Oxygen Vacancies in Magnetic Oxides. *Micron* **2000**, *31*, 571–580.
- (68) Hwang, S.; Chang, W.; Kim, S. M.; Su, D.; Kim, D. H.; Lee, J. Y.; Chung, K. Y.; Stach, E. a. Investigation of Changes in the Surface Structure of $\text{Li}_x\text{Ni}_{0.8}\text{Co}_{0.15}\text{Al}_{0.05}\text{O}_2$ Cathode Materials Induced by the Initial Charge. *Chem. Mater.* **2014**, *26*, 1084–1092.
- (69) Yoon, W.-S.; Chung, K. Y.; McBrenn, J.; Fischer, D. A.; Yang, X.-Q. Electronic Structural Changes of the Electrochemically Li-Ion Deintercalated $\text{LiNi}_{0.8}\text{Co}_{0.15}\text{Al}_{0.05}\text{O}_2$ Cathode Material Investigated by X-Ray Absorption Spectroscopy. *J. Power Sources* **2007**, *174*, 1015–1020.
- (70) Sallis, S.; Pereira, N.; Mukherjee, P.; Quackenbush, N. F.; Faenza, N.; Schlueter, C.; Lee, T.-L.; Yang, W. L.; Cosandey, F.; Amatucci, G. G.; Piper, L. F. J. Surface Degradation of

$\text{Li}_{1-x}\text{Ni}_{0.80}\text{Co}_{0.15}\text{Al}_{0.05}\text{O}_2$ Cathodes: Correlating Charge Transfer Impedance with Surface Phase Transformations. *Appl. Phys. Lett.* **2016**, *108*, 263902.

(71) Jung, S.-K.; Gwon, H.; Hong, J.; Park, K.-Y.; Seo, D.-H.; Kim, H.; Hyun, J.; Yang, W.; Kang, K. Understanding the Degradation Mechanisms of $\text{LiNi}_{0.5}\text{Co}_{0.2}\text{Mn}_{0.3}\text{O}_2$ Cathode Material in Lithium Ion Batteries. *Adv. Energy Mater.* **2014**, *4* (1), 1300787.

(72) Lin, F.; Markus, I. M.; Nordlund, D.; Weng, T.-C.; Asta, M. D.; Xin, H. L.; Doeff, M. M. Surface Reconstruction and Chemical Evolution of Stoichiometric Layered Cathode Materials for Lithium-Ion Batteries. *Nat. Commun.* **2014**, *5*, 3529.

(73) Yan, P.; Zheng, J.; Zheng, J.; Wang, Z.; Teng, G.; Kuppan, S.; Xiao, J.; Chen, G.; Pan, F.; Zhang, J.-G.; Wang, C.-M. Ni and Co Segregations on Selective Surface Facets and Rational Design of Layered Lithium Transition-Metal Oxide Cathodes. *Adv. Energy Mater.* **2016**, *6*, 1502455.

(74) Boulineau, A.; Simonin, L.; Colin, J.-F. o.; Carole, B.; Patoux, S. b. First Evidence of Manganese – Nickel Segregation and Densification upon Cycling in Li-Rich Layered Oxides for Lithium Batteries. *Nano Lett.* **2013**, *13*, 3857–3863.

(75) Gu, M.; Belharouak, I.; Zheng, J.; Wu, H.; Xiao, J.; Genc, A.; Amine, K.; Thevuthasan, S.; Baer, D. R.; Zhang, J. G.; Browning, N. D.; Liu, J.; Wang, C. Formation of the Spinel Phase in the Layered Composite Cathode Used in Li-Ion Batteries. *ACS Nano* **2013**, *7* (1), 760–767.

(76) Chebiam, R. V.; Prado, F.; Manthiram, A. Comparison of the Chemical Stability of $\text{Li}_{1-x}\text{CoO}_2$ and $\text{Li}_{1-x}\text{Ni}_{0.85}\text{Co}_{0.15}\text{O}_2$ Cathodes. *J. Solid State Chem.* **2002**, *163* (1), 5–9.

(77) Das, H.; Urban, A.; Huang, W.; Ceder, G. First-Principles Simulation of the (Li–Ni–Vacancy)O Phase Diagram and Its Relevance for the Surface Phases in Ni-Rich Li-Ion Cathode Materials. *Chem. Mater.* **2017**, *29*, 7840–7851.